Unifying theoretical framework for deciphering the oxygen reduction reaction on platinum

Jun Huang,[1,2,*] *Jianbo Zhang,*[2,3] *Michael Eikerling*[4]

[1] College of Chemistry and Chemical Engineering, Central South University, Changsha 410083, PR China
[2] Department of Automotive Engineering, State Key Laboratory of Automotive Safety and Energy, Tsinghua University, Beijing 100084, China
[3] Beijing Co-Innovation Center for Electric Vehicles, Beijing Institute of Technology, Beijing 100081, China
[4] Department of Chemistry, Simon Fraser University, Burnaby, BC V5A 1S6, Canada

* Corresponding author: jhuangelectrochem@qq.com

Final Version published as: J. Huang, J.Zhang and M. Eikerling. Unifying theoretical framework for deciphering the oxygen reduction reaction on platinum. *Physical Chemistry Chemical Physics*, 2018, DOI:10.1039/C8CP01315B.

ABSTRACT

Rapid conversion of oxygen into water is crucial to the operation of polymer electrolyte fuel cells and other emerging electrochemical energy technologies. Chemisorbed oxygen species play double-edged roles in this reaction, acting as vital intermediates on one hand and site-blockers on the other. Any attempt to decipher the oxygen reduction reaction (ORR) must first relate the formation of oxygen intermediates to basic electronic and electrostatic properties of the catalytic surface, and then link it to parameters of catalyst activity. An approach that accomplishes this feat will be of great utility for catalyst materials development and predictive model formulation of electrode operation. Here, we present a theoretical framework for the multiple interrelated surface phenomena and processes involved, particularly, by

incorporating the double-layer effects. It sheds light on the roles of oxygen intermediates and gives out the Tafel slope and exchange current density as continuous functions of electrode potential. Moreover, it develops the concept of a rate determining term which should replace the concept of a rate determining step for multi-electron reactions, and offers a new perspective on the volcano relation of the ORR.

TABLE OF ENTRY GRAPHICS

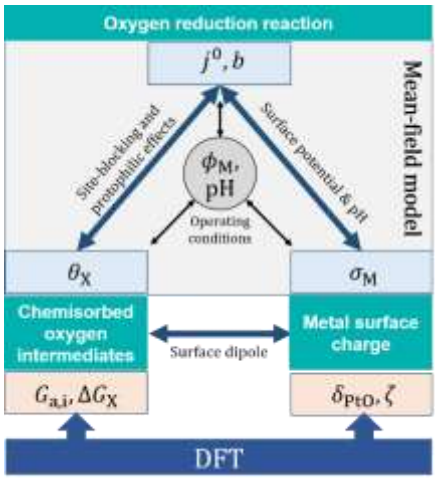

A theoretical framework relates formation of oxygen intermediates to basic electronic and electrostatic properties of the catalytic surface.

1 INTRODUCTION

Forays in materials research, electrode design, and theoretical electrocatalysis strive to unravel the molecular mechanism and kinetics of oxygen reduction and oxygen evolution reaction (ORR and OER). These reactions are of utmost importance for several emerging electrochemical energy technologies, including polymer electrolyte fuel cells (PEFCs), polymer electrolyte electrolysis cells and metal-air batteries. Scientifically, the ORR exemplifies an essential class of multielectron electrocatalytic reaction. Technologically, voltage losses incurred by the ORR pose a threat to the commercial prospects of PEFCs as they determine the platinum loading required to meet performance targets.

Progress in understanding of the ORR has been enabled by advances in experimentation, such as the preparation of Pt single crystals and surface analytical methods, and first-principles theoretical approaches, see recent reviews.[1-4] X-ray photoelectron spectroscopy (XPS) has been employed to identify chemisorbed oxygen intermediates on Pt single-crystal electrodes under ultra-high vacuum[5, 6] and at a Pt fuel cell cathode under operating conditions.[7] Different chemisorbed oxygen intermediates, viz., O* and OH*, were discerned. Recent efforts strive to elucidate detailed atomic-scale configurations and electrocatalytic reactivities of surface states modified by these intermediates.[8]

Quantum mechanical calculations based on density functional theory (DFT) have revealed that the ORR in acidic solution at relevant cathode potentials of fuel cell operation is likely to proceed via an associative mechanism involving O_2 adsorption and formation of an OOH* intermediate.[9-14] OOH*, thermodynamically unstable, dissociates spontaneously into O* and OH*, followed by electrochemical reduction

to water.[9-13] The binding energies of the chemisorbed oxygen intermediates are correlated and have been found to follow linear scaling relations.[15-17] Therefore, the adsorption energy of OH*, ΔG^0_{OH}, or the adsorption energy of O*, ΔG^0_{O}, emerges as the sole descriptor to display the ORR activity in so-called volcano plots.[1, 13] Volcano-shaped relations between catalytic activity and ΔG^0_{OH} have been exploited with some success in experimental-theoretical efforts to improve catalyst activity through alloying.[1, 13, 18]

What is the role of chemisorbed oxygen intermediates in the ORR? An oversimplified view assumes that chemisorbed oxygen intermediates act as site-blockers.[18, 19] This view leads to a relation between the ORR current, j_{ORR}, and the total coverage of chemisorbed oxygen intermediates, θ_{X}, of the type $j_{ORR} \propto (1-\theta_{\mathrm{X}})^n$ with n usually being taken as unity.[18, 20] This relation found partial empirical support in the improved ORR activity seen on $Pt_3Ni(111)$ as compared with Pt(111) that was interpreted as an effect of the decreased θ_{X}, in the spirit of the site-blocking hypothesis.[18, 20]

In addition to the site-blocking effect, Sepa *et al.* postulated that chemisorbed oxygen intermediates could incur a negative energetic effect by increasing the activation energy of reactions.[21-23] The site-blocking and negative energetic effects of chemisorbed oxygen intermediates were also invoked to interpret the experimentally observed transition of the Tafel slope from ~120 mV/dec in the high overpotential region, where the catalyst surface is free of chemisorbed oxygen intermediates, to <60 mV/dec in the low overpotential region, where chemisorbed oxygen intermediates are present.[22, 24, 25]

Wang *et al.* pointed out that it is overly simplistic to interpret the effect of chemisorbed oxygen intermediates as being site-blocking only.[24]

Watanabe and co-workers employed XPS to measure the coverage of OH^* and O^* on Pt(111), Pt(100) and Pt(110) in 0.1 M HF solution in the potential range of $0.6 - 1.0$ V relevant for PEFC operation.[5, 6] They did not find a correlation between the potential-dependent coverage of OH^* and ORR activities on these Pt surfaces. Their data thus do not support the site-blocking effect of OH^*.[3] Furthermore, Wakisaka *et al.* reported an enhanced ORR activity at Pt-Fe alloy with increased coverage of OH^*.[26] The Feliu group also questioned the negative roles of chemisorbed oxygen intermediates in the ORR.[4, 27, 28] Data from the Feliu group reveal that the ORR activity surprisingly increases on Pt single crystals with a higher coverage of chemisorbed oxygen intermediates.[4]

To summarize, there seems to be ample evidence for the site-blocking effect and the negative energetic effect due to chemisorbed oxygen intermediates. However, positive effects may mask or overcompensate the negative ones. Therefore, the complex roles of chemisorbed oxygen intermediates in the ORR have thus remained elusive. One should thus refrain from the inclination to condense the high-dimensional parameter space that governs the ORR activity into a single descriptor, namely the oxide coverage or the adsorption energy of a specific chemisorbed oxygen intermediate.

A positive effect of chemisorbed oxygen intermediates may be related to the protophilicity that they induce. The surface layer of chemisorbed oxygen species tends to increase the proton affinity of the Pt surface, as revealed in prior theoretical work.[29] By means of a refined structural model of the electrified interface the theory revealed the peculiar non-monotonic charging relation of Pt that had been seen earlier in experimental studies by Frumkin and Petrii.[30] The free metal surface charge density, σ_M, exhibits consecutive transitions from negative to

positive and again to negative upon transitioning the metal phase potential from the hydrogen adsorption region ($0 - 0.5$ V, vs NHE) to the double layer charging region ($0.5 - 0.8$ V vs NHE) and further to the oxide formation region (> 0.8 V vs NHE).[29] The interfacial proton density is bound to follow the trend in σ_M. For a water-filled Pt nanopore, our work revealed that the proton concentration in the potential region of oxide formation can be up to six orders higher than that of pure water.[31] It is thus to be expected that the ORR activity is greatly facilitated by the protophilicity effect induced by chemisorbed oxygen species.

Chemisorbed oxygen intermediates will thus exert a strong impact on the surface activity for the ORR. The challenge in unraveling this behavior is to treat the formation of chemisorbed oxygen intermediates, surface charging, field-dependent orientational ordering of interfacial water molecules, distribution of proton density and potential in electrolyte phase, and mechanism and kinetics of the ORR in a self-consistent manner. The control variable to steer this complex interplay is the *metal phase potential*, as realized in experiment but difficult to emulate in computational studies that employ density functional theory, as discussed in a recent perspective article.[2] The work presented in this article follows a less ambitious route as it strives to develop a versatile framework that rests upon a mean field-type description of the electrochemical interface, while incorporating specific microscopic information obtained from DFT as well as analyses of experimental data to determine essential input parameters of the model.

The remainder of this article is organized as follows. Section 2 formulates the theoretical framework. In section 3, we parameterize the model, examine the effect of surface charge on the ORR, analyze the rate-determining terms in the ORR rate expression, calculate the

differential Tafel slope and exchange current density, and close the section with the calculation of an experimental volcano plot, based on the presented parameterization of the model. In section 4, we scrutinize the root causes of the volcano-type relation, followed by dwelling upon the relation between ORR activity and the coverage of chemisorbed oxygen intermediates and picking out key parameters of the ORR model.

2 THEORETICAL FRAMEWORK

Figure 1 illustrates the theoretical framework and the interplay between different components of the theory. In the presented model, DFT calculations play a vital role in identifying the thermodynamically stable configuration of the oxidized metal surface, calculating Gibbs energies of reaction and activation for elementary steps along the reaction pathway of the ORR, and determining microscopic parameters of the dipole layer formed by chemisorbed oxygen species.[9, 12, 13] Given the reaction pathway and Gibbs energies, kinetic equations of the elementary steps of the ORR are expressed. Under steady state, the surface coverage of chemisorbed oxygen intermediates and the ORR rate can be calculated as functions of interfacial reaction conditions, which are dictated by the metal surface charge density. Following that, the surface oxide dipole can be calculated based on the surface coverage of chemisorbed oxygen intermediates.

Given microscopic parameters of the double layer obtained from DFT and the surface oxide dipole density and its associated electric field, a mean-field electrochemical interface model results in the metal surface charge density as a function of electrode potential and solution properties, which in turn determines the interfacial reaction conditions in the ORR rate expression.

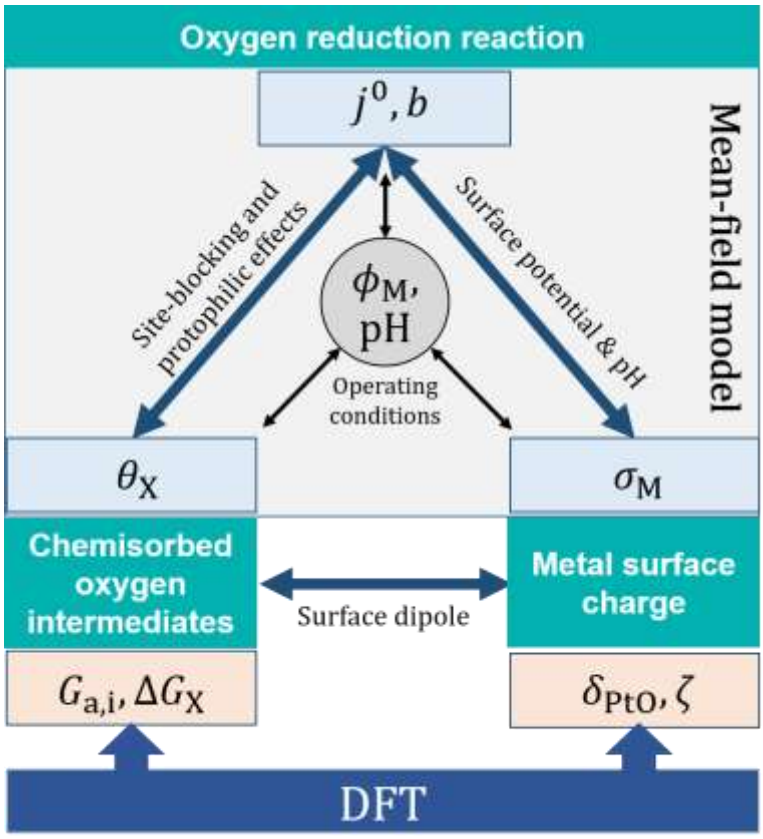

Figure 1. Interplay of chemisorbed oxygen intermediates, metal surface charge, and ORR activity. Microscopic information, such as the reaction pathway of the ORR, Gibbs energies of adsorption of intermediates, Gibbs energies of activation of elementary steps, and structure and dipolar properties of the of the chemisorbed oxide layer, are obtained from DFT. Parameters seen in the figure are explained in the text.

2.1 Postulated mechanism of the ORR

Reaction mechanisms of the ORR fall into two broad classes, referred to as dissociative and associative mechanism.[4, 9, 32] In the dissociative mechanism, an adsorbed oxygen molecule on the metal surface first dissociates into two adsorbed oxygen atoms, O*, via cleavage of the O-O bond, followed by reduction to OH*. DFT studies have reported that the dissociation barrier of O_2 is as high as ~0.6 eV, rendering this

process an unlikely reaction step.[12, 33, 34]

More likely is the associative mechanism, in which the O-O bond is preserved upon adsorption.[12, 13, 34] The reaction pathway proceeds in at least four steps, which according to the mechanism proposed in refs 9, 13 are,

$$O_2 + H^+ + e^- + * \leftrightarrows OOH*, \qquad \text{(Step 1)}$$

$$OOH* + * \leftrightarrows OH* + O*, \qquad \text{(Step 2)}$$

$$O* + H^+ + e^- \leftrightarrows OH*, \qquad \text{(Step 3)}$$

$$2(OH* + H^+ + e^-) \leftrightarrows 2H_2O + 2*. \qquad \text{(Step 4)}$$

where the asterisks indicate adsorbed reaction intermediates.

XPS studies showed that the $OOH*$ coverage is negligible, $\theta_{OOH} \approx 0$.[5, 6] Consistently, DFT studies also indicated that $OOH*$ is unstable and spontaneously dissociates into $OH*$ and $O*$.[34] As an alternative to Step 2, $OOH*$ could be reduced in an electrochemical step,[13]

$$OOH* + H^+ + e^- \leftrightarrows O* + H_2O, \qquad \text{(Step 2')}$$

followed by step 3 and 4. What follows is based on the associative mechanism consisting of step 1-4. Similar treatment could be applied to other pathways.

2.2 Thermodynamics

The Gibbs reaction and activation energy of step i, ΔG_i and $G_{a,i}$, can be calculated with the help of DFT, as demonstrated in refs 12, 13. These free energies depend on the state of the system. We will indicate standard state (298K, 1 bar pressure, pH = 0) by a superscript "0" and the equilibrium state by a superscript 'eq'.

ΔG_i is calculated from the Gibbs free energies ΔG_X of reaction intermediates, X, involved in step i. ΔG_X on the Pt(111) electrode at the

standard state and $\mathrm{U} = 0$ V (SHE) is denoted as $\Delta G_{\mathrm{X}}^{\mathrm{Pt,0}}$. Table 1 lists values of $\Delta G_{\mathrm{X}}^{\mathrm{Pt,0}}$, calculated from DFT studies.[12, 13] Given the values of $\Delta G_{\mathrm{X}}^{\mathrm{Pt,0}}$, we can determine the equilibrium potential $E_{\mathrm{i}}^{\mathrm{eq}}$ of step 1,3 and 4 at the standard state using the Nernst equation,

$$E_{\mathrm{i}}^{\mathrm{eq}} = -\frac{\Delta G_{\mathrm{i}}^{0}}{\mathrm{e}}, \mathrm{i} = 1,3,4. \quad (1)$$

The results are shown in Table 2.

The values of ΔG_{X} vary among different facets of Pt single crystals and they are modified by subsurface alloying.[1, 18] DFT studies have revealed that ΔG_{X} values of different chemisorbed oxygen intermediates on a given catalyst surface are correlated.[10, 13, 16] At the standard state, scaling relations can be written as,

$$\Delta G_{\mathrm{X}}^{0} = \Delta G_{\mathrm{X}}^{\mathrm{Pt,0}} + \zeta_{\mathrm{X}}\left(\Delta G_{\mathrm{OH}}^{0} - \Delta G_{\mathrm{OH}}^{\mathrm{Pt,0}}\right), \quad (2)$$

with $\Delta G_{\mathrm{OH}}^{0}$ being the standard adsorption energy of OH*, which could be employed as the single independent descriptor of the ORR activity, and ζ_{X} being the scaling coefficient for species X.

Departure from equilibrium potential E_i^{eq} incurs shifts in reaction Gibbs energies,

$$\Delta G_1 = F\left(E - E_1^{\mathrm{eq}}\right), \quad (3)$$

$$\Delta G_3 = F\left(E - E_3^{\mathrm{eq}}\right) + \delta G_{\mathrm{OH}} - \delta G_{\mathrm{O}}, \quad (4)$$

$$\Delta G_4 = F\left(E - E_4^{\mathrm{eq}}\right) - \delta G_{\mathrm{OH}}, \quad (5)$$

where E is the potential difference between the metal and the reaction plane in solution, δG_{OH} and δG_{O} represent variations in Gibbs free energies of $\mathrm{OH}*$ and $\mathrm{O}*$ due to variations in coverages,[22]

$$\delta G_{\mathrm{OH}} = \xi_{\mathrm{OH}}\left(\theta_{\mathrm{OH}} - \theta_{\mathrm{OH}}^{\mathrm{eq}}\right), \tag{6}$$

$$\delta G_{\mathrm{O}} = \xi_{\mathrm{O}}\left(\theta_{\mathrm{O}} - \theta_{\mathrm{O}}^{\mathrm{eq}}\right), \tag{7}$$

with θ_{O} and θ_{OH} being the coverages at E, $\theta_{\mathrm{OH}}^{\mathrm{eq}}$ and $\theta_{\mathrm{O}}^{\mathrm{eq}}$ being the coverages at E_i^{eq}, and ξ_{OH} and ξ_{O} being lateral interaction parameters. Previous modeling studies[13, 35] assumed that adsorbate interaction effects are negligible, that is, $\xi_{\mathrm{OH}} = \xi_{\mathrm{O}} = 0$, corresponding to Langmuir adsorption conditions. Here we consider adsorbate interactions corresponding to Frumkin adsorption conditions.

The Bronsted-Evans-Polanyi (BEP) relation implies a linear relation between the variations in $G_{\mathrm{a,i}}$ and the variations in ΔG_{i}.[13] Therefore, we write,

$$\mathrm{G_{a,i}} = G_{\mathrm{a,i}}^{\mathrm{eq}} + \beta_i \Delta G_{\mathrm{i}}, \tag{8}$$

$$G_{\mathrm{a,-i}} = G_{\mathrm{a,-i}}^{\mathrm{eq}} - (1 - \beta_i)\Delta G_{\mathrm{i}}, \tag{9}$$

where $G_{\mathrm{a,i}}^{\mathrm{eq}}$ and $G_{\mathrm{a,-i}}^{\mathrm{eq}}$ are activation energies of step i under equilibrium at the standard state for the forward and backward reactions, respectively, and β_i is the transfer coefficient. Note that the relations $G_{\mathrm{a,-i}}^{\mathrm{eq}} = G_{\mathrm{a,i}}^{\mathrm{eq}} - \Delta G_{\mathrm{i}}^{\mathrm{eq}}$ and $G_{\mathrm{a,-i}}^{\mathrm{eq}} = G_{\mathrm{a,i}}^{\mathrm{eq}}$ hold in equilibrium as we have $\Delta G_{\mathrm{i}}^{\mathrm{eq}} = 0$.

Table 1. Standard free energy of reaction intermediates on Pt(111), $\Delta G_{\mathrm{X}}^{\mathrm{Pt,0}}$, scaling coefficient, ζ_{X}, and lateral interaction coefficient, $\xi_{\mathrm{X}}^{\mathrm{Pt}}$.

X	$\Delta G_{\mathrm{X}}^{\mathrm{Pt,0}}$ / eV	ζ_{X}	$\xi_{\mathrm{X}}^{\mathrm{Pt}}$ / $\mathrm{kJ \cdot mol^{-1}}$
O_2	4.92	-	-
OOH	3.91	1	-
OH	0.75	1	0~20

0	1.7	2	0~20

Note:

(1) Values of $\Delta G_{\mathrm{X}}^{\mathrm{Pt},0}$ and ζ_{X} are taken from DFT studies.[12, 13]

(2) Values of $\xi_{\mathrm{X}}^{\mathrm{Pt}}$ are scarce in the literature. Reference 36 reported $\xi_{\mathrm{OH}} = 13.3\ \mathrm{kJ \cdot mol^{-1}}$ for Pt(111). Reference 37 reported a coverage-dependent ξ_{OH} that decreased from 15 $\mathrm{kJ \cdot mol^{-1}}$ to $-10\mathrm{kJ \cdot mol^{-1}}$ with θ_{OH} increasing from 0 to 0.8. DFT calculation in ref [38] reported $\xi_{\mathrm{OH}} = 115.6\ \mathrm{kJ \cdot mol^{-1}}$ in the θ_{OH} range of [0.1, 1], while DFT calculation in ref 12 showed a weakly negative dependence of $\Delta G_{\mathrm{OH}}^{\mathrm{Pt},0}$ on θ_{OH} in the range of [0, 0.3].

Table 2. Standard equilibrium potential, $E_{\mathrm{i}}^{\mathrm{eq}}$, activation free energy, $G_{\mathrm{a,i}}^{\mathrm{eq}}$, and transfer coefficient, β_i of elementary step i.

Step	$\Delta G_{\mathrm{i}}^{0}$ / eV	$E_{\mathrm{i}}^{\mathrm{eq}}$ / V	$G_{\mathrm{a,i}}^{\mathrm{eq}}$ / eV	β_i
1	$\Delta G_{\mathrm{OOH}}^{0} - \Delta G_{\mathrm{O_2}}^{0}$	1.01	0.37	0.5
3	$\Delta G_{\mathrm{OH}}^{0} - \Delta G_{\mathrm{O}}^{0}$	0.95	0.26	0.5
4	$-\Delta G_{\mathrm{OH}}^{0}$	0.75	0.26	0.5

Note:

(1) Values of $\Delta G_{\mathrm{i}}^{0}$ and $E_{\mathrm{i}}^{\mathrm{eq}}$ are calculated using values in Table 1.

(2) Values of $G_{\mathrm{a,i}}^{\mathrm{eq}}$ and β_i are taken from DFT studies.[12, 13]

2.3 Kinetics

The rate equations for the elementary steps are given by,

$$v_1 = k_1[\mathrm{O_2}][\mathrm{H^+}](\theta_{max} - \theta_{\mathrm{O}} - \theta_{\mathrm{OH}} - \theta_{\mathrm{OOH}}) - k_{-1}\theta_{\mathrm{OOH}}, \qquad (10)$$

$$v_2 = k_2\theta_{\mathrm{OOH}}(\theta_{max} - \theta_{\mathrm{O}} - \theta_{\mathrm{OH}} - \theta_{\mathrm{OOH}}) - k_{-2}\theta_{\mathrm{O}}\theta_{\mathrm{OH}}, \quad (11)$$

$$v_3 = k_3[\mathrm{H}^+]\theta_{\mathrm{O}} - k_{-3}\theta_{\mathrm{OH}}, \quad (12)$$

$$v_4 = k_4[\mathrm{H}^+]\theta_{\mathrm{OH}} - k_{-4}(\theta_{max} - \theta_{\mathrm{O}} - \theta_{\mathrm{OH}} - \theta_{\mathrm{OOH}}), \quad (13)$$

where θ_{max} is the maximum coverage of chemisorbed oxygen intermediates, $[\mathrm{O}_2] = c_{\mathrm{O}_2}^{\mathrm{aq}}/c_{\mathrm{O}_2}^{ref}$ is the dimensionless oxygen concentration, $[\mathrm{H}^+] = c_{\mathrm{H}^+}^{surf}/c_{\mathrm{H}^+}^{ref}$ is the dimensionless proton concentration at the reaction plane. Here, we use $c_{\mathrm{O}_2}^{ref} = 40.3$ mol/m^3 (corresponding to 1 atm), and $c_{\mathrm{H}^+}^{ref} = 1000$ mol/m^3. k_{i} and $k_{-\mathrm{i}}$ are rate constants given by,

$$k_{\pm\mathrm{i}} = k_{\mathrm{i}}^0 \exp\left(-\frac{G_{\mathrm{a},\pm\mathrm{i}}}{RT}\right), \quad (14)$$

where $k_i^0 = k_{\mathrm{B}}T/h$ is a prefactor with k_{B} being Boltzmann constant and h Planck constant. Equilibrium constants K_{i} are expressed as, $K_{\mathrm{i}} = k_{\mathrm{i}}/k_{-\mathrm{i}}$.

Henry law is employed to calculate the concentration of dissolved oxygen in the aqueous solution,

$$c_{\mathrm{O}_2}^{\mathrm{aq}} = c_{\mathrm{O}_2}^{\mathrm{gas}} H_{O_2}, \quad (15)$$

with the oxygen concentration in the gas phase $c_{\mathrm{O}_2}^{\mathrm{gas}}$ and Henry constant of oxygen, H_{O_2}. $H_{O_2} = 0.032$ at 25℃.

In the steady state, reaction rates must fulfill the following balance, $v_{\mathrm{ORR}} = v_1 = v_3 = v_4/2$. Using this relation and the assumption of $\theta_{\mathrm{OOH}} \approx 0$,[2, 5, 6, 34] we can solve for θ_{O}, θ_{OH} and v_{ORR},

$$\frac{\theta_{\mathrm{OH}}}{\theta_{max}} = \frac{(K_4^* k_1^*)^{-1} + (k_4^*/2)^{-1}}{(k_1^*)^{-1} + (k_3^*)^{-1} + (k_4^*/2)^{-1} + (K_4^* k_1^*)^{-1} + (K_3^* k_4^*/2)^{-1} + (K_3^* K_4^* k_1^*)^{-1}}, \quad (16)$$

$$\frac{\theta_{\mathrm{O}}}{\theta_{max}} = \frac{(k_3^*)^{-1} + (K_3^* k_4^*/2)^{-1} + (K_3^* K_4^* k_1^*)^{-1}}{(k_1^*)^{-1} + (k_3^*)^{-1} + (k_4^*/2)^{-1} + (K_4^* k_1^*)^{-1} + (K_3^* k_4^*/2)^{-1} + (K_3^* K_4^* k_1^*)^{-1}}, \quad (17)$$

$$\frac{\theta_{max}}{v_{ORR}} = (k_1^*)^{-1} + (k_3^*)^{-1} + (k_4^*/2)^{-1} + (K_4^* k_1^*)^{-1} + (K_3^* k_4^*/2)^{-1} + (K_3^* K_4^* k_1^*)^{-1}, \quad (18)$$

where $k_1^* = k_1[O_2][H^+], k_3^* = k_3[H^+], k_4^* = k_4[H^+]$ are rate constants that are dependent on the reactant concentrations and $K_3^* = k_3^*/k_{-3}, K_4^* = k_4^*/k_{-4}$ are corresponding equilibrium constants.

The ORR current, j_{ORR}, is given by,[13]

$$j_{\mathrm{ORR}} = v_{\mathrm{ORR}} \cdot e\rho, \quad (19)$$

where e is elementary charge, ρ surface density of Pt atoms. $e\rho = 2.41\ \mathrm{C/m^2}$.[13]

2.4 Coverage of chemisorbed oxygen intermediates

The rate constants k_{i} depend on the interfacial potential $E^{\mathrm{surf}} = \phi_{\mathrm{M}} - \phi_{\mathrm{S}}^{\mathrm{surf}}$, where $\phi_{\mathrm{S}}^{\mathrm{surf}}$ is the interfacial potential at the outer Helmholtz plane (OHP) in solution, and on the interfacial proton concentration, $c_{\mathrm{H^+}}^{\mathrm{surf}}$. As discussed in the next subsection, $\phi_{\mathrm{S}}^{\mathrm{surf}}$ and $c_{\mathrm{H^+}}^{\mathrm{surf}}$ are functions of σ_{M}. Using Boltzmann relation we can replace $\phi_{\mathrm{S}}^{\mathrm{surf}}$ and $c_{\mathrm{H^+}}^{\mathrm{surf}}$ with the bulk values $\phi_{\mathrm{S}}^{\mathrm{b}}$ and $c_{\mathrm{H^+}}^{\mathrm{b}}$, respectively, to express θ_{O}, θ_{OH} and v_{ORR} as functions of the electrode potential $E = \phi_{\mathrm{M}} - \phi_{\mathrm{S}}^{\mathrm{b}}$, where $\phi_{\mathrm{S}}^{\mathrm{b}}$ is the bulk solution phase potential at standard conditions, and of the pH in solution.[29]

Figure 2 compares experimental data of the coverage of the intermediates with model results. Experimental data were measured using the XPS technique on a Pt(111) electrode in 0.1 M N_2-saturated HF solution.[5, 6] In this scenario, we have $[0_2] = 0$. Gibbs reaction energies used in the model simulation are taken from DFT studies as

listed in Table 1. Free parameters used in the model fitting are ξ_{OH}, ξ_O and θ_{max}. By using $\xi_{OH} = 10$ kJ mol^{-1}, $\xi_O = 10$ kJ mol^{-1}, and $\theta_{max} = 0.4$, a good match in terms of θ_{OH} and θ_O between experiment and model is achieved. The formation of $OH*$ commences at ~ 0.6 V, followed by the transformation into $O*$ above 0.8 V. θ_{OH} and θ_O calculated from DFT and Monte Carlo simulations by Casalongue *et al.* exhibited similar trends.[7]

The effect of lateral interaction coefficient ξ_X on θ_X is examined in Figure S1. It is found that increasing ξ_{OH} from 0 kJ mol^{-1} to 20 kJ mol^{-1} increases the width of the peak of θ_{OH}. Increasing ξ_O from 0 kJ mol^{-1} to 20 kJ mol^{-1} decreases θ_O, while increases θ_{OH}, in the potential range of [0.8, 1.2] V. Albeit being in line with the range given in Table 1, the obtained values of ξ_{OH} and ξ_O have a large confidence interval due to the low sensitivity of the coverages to ξ_{OH} and ξ_O, as seen in Figure S1.

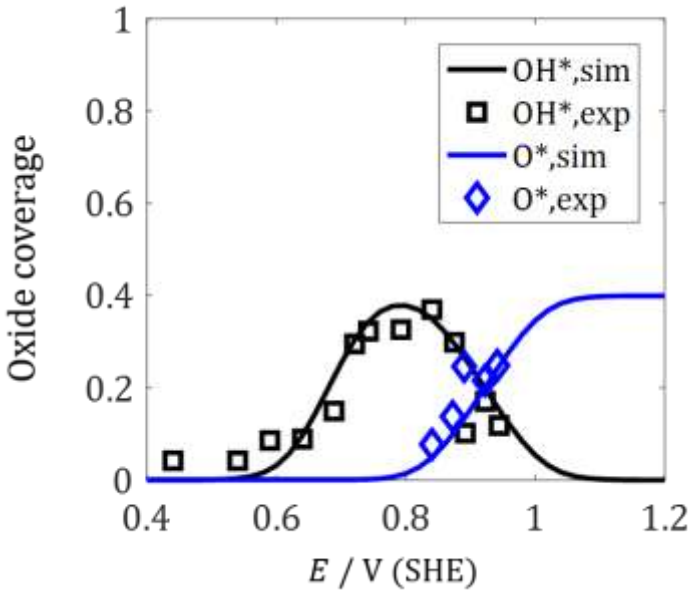

Figure 2. Comparison between experimental data and model simulation in terms of the coverage of adsorbed intermediates on

Pt(111) in 0.1 M N_2-saturated HF solution. Experimental data were determined from XPS analysis in refs 5, 6. Note that experimental data were presented in RHE scale in the original paper and they are transformed to the SHE scale here.

2.5 Metal surface charge

As mentioned before, $E^{\mathrm{surf}} = \phi_{\mathrm{M}} - \phi_{\mathrm{S}}^{\mathrm{surf}}$ and $[\mathrm{H}^+] = c_{\mathrm{H}^+}^{\mathrm{surf}}/c_{\mathrm{H}^+}^{\mathrm{ref}}$. Therefore, determination of $\phi_{\mathrm{S}}^{\mathrm{surf}}$ and $c_{\mathrm{H}^+}^{\mathrm{surf}}$ constitutes a precondition to calculate v_{ORR} and j_{ORR}. For this purpose, we must first find σ_{M}.

σ_{M} can be derived from the refined structural model of electrified interfaces, as described in detailed in ref 29. This approach, which includes oxide layer and water layer sub-models, gives

$$\frac{2RT}{F}\operatorname{arsinh}\left(\frac{F\lambda_{\mathrm{D}}\sigma_{\mathrm{M}}}{2RT\epsilon_{\mathrm{S}}}\right) + \sigma_{\mathrm{M}}\left(\frac{\delta_{\mathrm{OHP}}}{\epsilon_{\mathrm{OHP}}} + \frac{\delta_{\mathrm{IHP}}}{\epsilon_{\mathrm{IHP}}}\right) = \phi_{\mathrm{M}} - \Delta\phi_{\mathrm{M}} - \frac{\mu_{\mathrm{PtO}}}{\epsilon_{\mathrm{PtO}}} + \frac{N_{\mathrm{tot}}\mu_{\mathrm{w}}}{\epsilon_{\mathrm{IHP}}}\tanh(X), \tag{20}$$

where λ_{D} is the Debye length, $\lambda_{\mathrm{D}} = \sqrt{\varepsilon_{\mathrm{S}}RT/2F^2c_{\mathrm{tot}}}$, with c_{tot} being the total ion concentration in solution, ϵ_{S} the permittivity of the electrolyte solution, $\Delta\phi_{\mathrm{M}}$ a constant potential drop at the metal surface due to the electron spillover, ϵ_{PtO} the permittivity of the Pt oxide layer, ϵ_{IHP} and δ_{IHP} the permittivity and thickness of the inner Helmholtz plane (IHP), respectively, ϵ_{OHP} and δ_{OHP} the permittivity and thickness of the outer Helmholtz plane (OHP), respectively, N_{tot} the Pt atom density, and μ_{w} the water dipole moment. The variable X represents the dimensionless total field-dependent adsorption energy of water molecules. Using the two-state model adopted from ref 39, the following relation for the field-dependent behavior of interfacial water molecules is obtained,

$$\left(\frac{0.6}{\pi\delta_{\mathrm{IHP}}^2}+N_{\mathrm{tot}}\right)\frac{N_{\mathrm{A}}\mu_{\mathrm{w}}^2}{\delta_{\mathrm{IHP}}\epsilon_{\mathrm{IHP}}RT}\tanh(X)-X=\frac{N_{\mathrm{A}}\mu_{\mathrm{w}}\sigma_{\mathrm{M}}}{\epsilon_{\mathrm{IHP}}RT}, \quad (21)$$

with Avogadro number N_{A}.

In Eq. (20), μ_{PtO}, is the interfacial oxide dipole moment. $0\mathrm{H}*$ and $0*$ are co-existing in an intermediate potential range, and we assume that the thickness of the oxide layer, δ_{PtO}, is the same for $0\mathrm{H}*$ and $0*$. Then

$$\mu_{\mathrm{PtO}}=N_{\mathrm{tot}}\cdot(\theta_{\mathrm{O}}\cdot\varsigma_{\mathrm{O}}e+\theta_{\mathrm{OH}}\cdot\varsigma_{\mathrm{OH}}e)\cdot\delta_{\mathrm{PtO}}, \quad (22)$$

with average charge numbers of oxygen species, ς_{O} and ς_{OH}. A simplified treatment assumes $\varsigma_{\mathrm{O}}=2\varsigma_{\mathrm{OH}}$. Table S1 lists the parameters of the electrified interface that are adopted from ref 29 which are updated according to recent DFT work.[38]

After determining σ_{M}, we can calculate $\phi_{\mathrm{S}}^{\mathrm{surf}}$ and $c_{\mathrm{H^+}}^{\mathrm{surf}}$ via the Poisson-Boltzmann equation,

$$\phi_{\mathrm{S}}^{\mathrm{surf}}=\frac{2RT}{F}\cdot\mathrm{arsinh}\left(\frac{\lambda_{\mathrm{D}}F\sigma_{\mathrm{M}}}{2\varepsilon_{\mathrm{S}}RT}\right), \quad (23)$$

$$c_{\mathrm{H^+}}^{\mathrm{surf}}=c_{\mathrm{H^+}}^{\mathrm{b}}\cdot\exp\left(-\frac{F\phi_{\mathrm{S}}^{\mathrm{surf}}}{RT}\right), \quad (24)$$

where, $c_{\mathrm{H^+}}^{\mathrm{b}}$ the bulk proton concentration. By substituting Eqs.(23)-(24) into $E^{\mathrm{surf}}=\phi_{\mathrm{M}}-\phi_{\mathrm{S}}^{\mathrm{surf}}$ and $[\mathrm{H^+}]=c_{\mathrm{H^+}}^{\mathrm{surf}}/c_{\mathrm{H^+}}^{\mathrm{ref}}$, we can calculate the ORR rate in Eq.(18) as a function of E and pH.

3 RESULTS

In this section, the model is parameterized using experimental data measured in rotating disk electrode (RDE) tests. Afterwards, making use of the basic set of parameters, we explore: (1) how θ_{O}, θ_{OH}, σ_{M}, and

$c_{H^+}^{surf}$ vary as functions of E; (2) how σ_M affects the current density of the ORR; (3) what reaction term determines the overall rate of the ORR; (4) how Tafel slope and exchange current density of the ORR change as functions of E. Moreover, we will evaluate results in a wider context by comparison to experimentally derived volcano plots.

3.1 Model parameterization

Figure 3 (a) compares model results and experimental data taken from ref 28. Experiments were conducted on a Pt(111) electrode in 0.1 M $NaF/\ HClO_4$ electrolyte saturated with O_2 at 1 bar and room temperature. In this case, $[O_2] = 0.032$. Three pHs, namely pH=1.2, 2.1, 4.3, were examined. The comparison between model and experiment is limited to the kinetically controlled potential regime, viz., in the potential range above 0.85 V (RHE). As the pH effect is investigated, the SHE potential scale is used in Figure 3.[40]

Model parameters in producing Figure 3 are explained below. Parameters of the Pt-solution interface are listed in Table S1, which are inherited from ref 29. $\xi_{OH} = 10\ \text{kJ mol}^{-1}$, $\xi_O = 10\ \text{kJ mol}^{-1}$ and $\theta_{max} = 0.4$ are adopted from the fitting of the coverage of chemisorbed oxygen species in section 2.4. The adjusted parameters are binding energies $\Delta G_X^{Pt,0}$ and activation free energy of the first step $G_{a,1}^{eq}$. Other thermodynamic and kinetic parameters of the ORR are adopted from DFT studies as shown in Table 1 and 2. At pH = 1.2, good agreement between model and experiment is achieved with $\Delta G_{OOH}^{Pt,0} = 4.02\ \text{eV}$, $\Delta G_{OH}^{Pt,0} = 0.92\ \text{eV}$, $\Delta G_O^{Pt,0} = 1.90\ \text{eV}$ and $G_{a,1}^{eq} = 0.52\ \text{eV}$. These energetic parameters deviate from their base values in Table 1 and 2 by a magnitude less than 0.2 eV, which is within the uncertainty range of DFT calculation of electrochemical interfaces.[41] For pH = 2.1 and pH =

4.3 the binding energy of OOH* $\Delta G_{\mathrm{OOH}}^{\mathrm{Pt},0}$ decreases to 3.97 and 3.84 eV, respectively, while the other three parameters keep unaltered.

Figure 3 shows the surface charge density and the surface reaction conditions, $c_{\mathrm{H^+}}^{\mathrm{surf}}$ and $\phi_{\mathrm{S}}^{\mathrm{surf}}$, as functions of E at pH = 1.2. σ_{M} increases in the potential range of $0.6\ \mathrm{V} < E < 0.78\ V$. At higher potentials, $E > 0.78\ V$, σ_{M} decreases. A transition to a second negative regime of σ_{M} occurs at $E = \ 0.92\ V$. The decline in σ_{M} when $E > 0.78\ V$ is caused by the increasing dipole field due to progressive formation surface oxides, as discussed in ref 29. Electrostatic interactions between the charged metal surface and ions in solution determine $c_{\mathrm{H^+}}^{\mathrm{surf}}$ and $\phi_{\mathrm{S}}^{\mathrm{surf}}$. $c_{\mathrm{H^+}}^{\mathrm{surf}}$ first decreases then increases when E increases from 0.6 V to 1.0 V. $\phi_{\mathrm{S}}^{\mathrm{surf}}$ exhibits a similar trend as σ_{M}, according to Eq.(23).

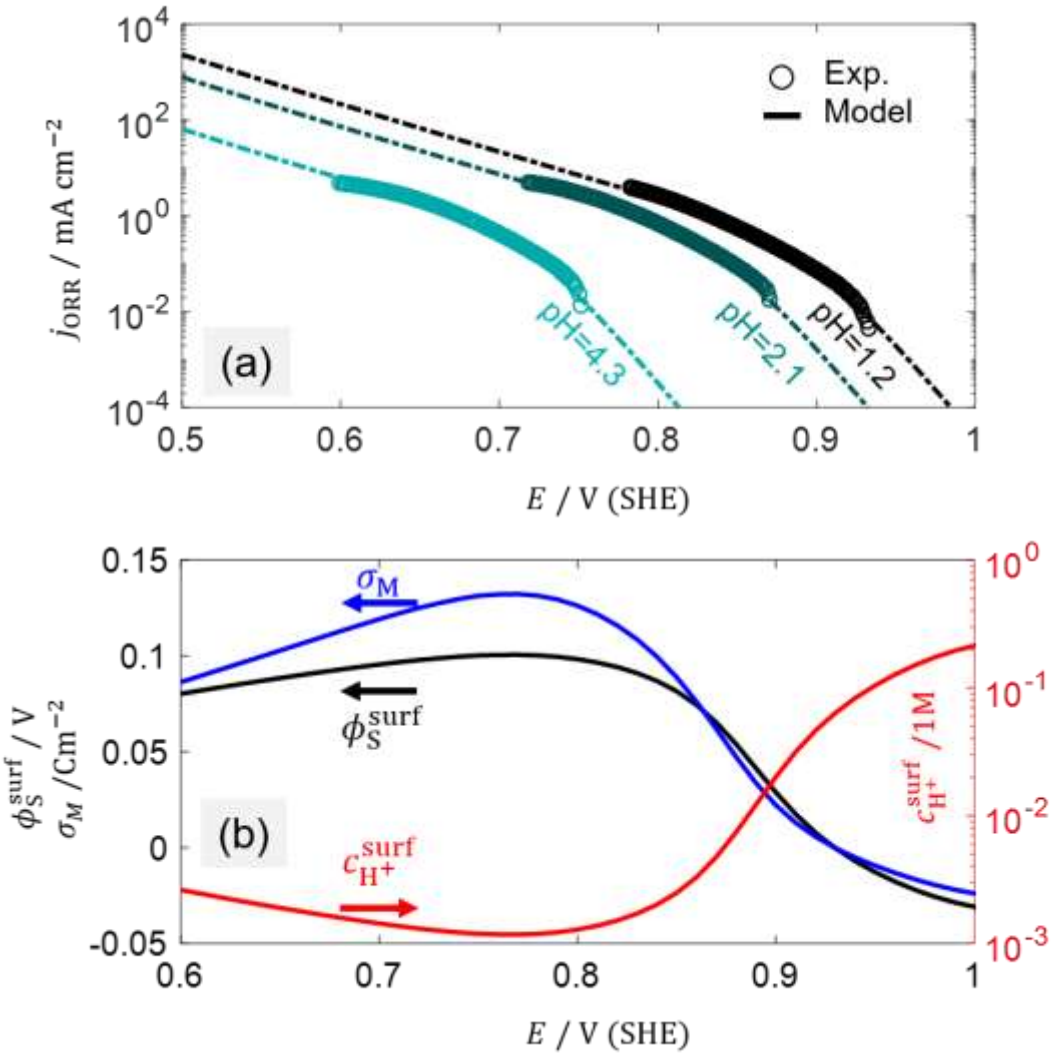

Figure 3. (a) Comparison between model and experiment in terms of the ORR current at three pHs. The ORR current density is normalized to the value at 0.95 V (RHE). The experimental data were measured using the RDE technique (2500 rpm) on a Pt(111) electrode in NaF/ $HClO_4$ electrolyte saturated with 0_2 of 1 bar at room temperature.[28] Three binding energies and one activation free energy were adjusted in model simulation. Other parameters have their base values. (b) Variation of σ_M and surface reaction conditions, $c_{H^+}^{surf}$ and ϕ_S^{surf} as functions of ϕ_M at pH=1.2.

3.2 Effect of surface charge

Figure 4 examines the effect of free metal surface charge density on ORR current density. For comparison, results are shown also for the case without surface charge effect, $\sigma_{\mathrm{M}} = 0$. In this case, pH=1.2, and correspondingly, $\Delta G_{\mathrm{OOH}}^{\mathrm{Pt},0} = 4.02$ eV, $\Delta G_{\mathrm{OH}}^{\mathrm{Pt},0} = 0.92$ eV and $\Delta G_{\mathrm{O}}^{\mathrm{Pt},0} = 1.90$ eV are used. According to Eq.(18), $j_{\mathrm{ORR}} \propto [\mathrm{H}^+]^{\gamma_{\mathrm{H}^+}}$ with $\gamma_{\mathrm{H}^+} > 0$, that is, the ORR current density will increase when more protons accumulate at the reaction plane driven by negative σ_{M}. From Figure 3 (b), σ_{M} transitions from positive to negative value at $E = 0.92\ V$ for the case of pH = 1.2. Consequently, the surface charge effect improves the ORR activity when $E > 0.92\ V$, as shown in Figure 4. The transition potential is dictated by $\Delta G_{\mathrm{OH}}^{\mathrm{Pt},0}$; specifically, it is lower when $\Delta G_{\mathrm{OH}}^{\mathrm{Pt},0}$ is smaller. The partial charge numbers of surface oxide species, ς_{OH} and ς_{O}, are key parameters dictating the surface charge effect in the oxide formation regime, as detailed in section 4.3.

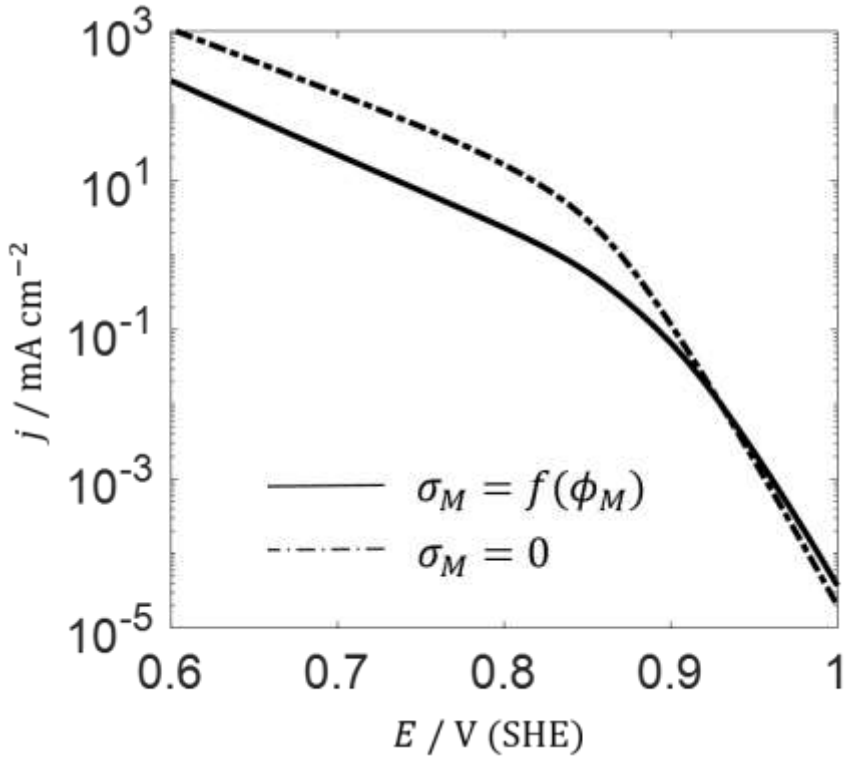

Figure 4. Effect of surface charge on the intrinsic ORR current density. Model calculation corresponds to a Pt(111) electrode in 0.1M $HClO_4$ electrolyte (pH=1.2) saturated with O_2 of 1 bar at room temperature. Dash-dotted lines correspond to cases without surface charge effect, $\sigma_M = 0$. Model parameters are the same as in Figure 3.

3.3 Rate-determining term

In Eq. (18), $(v_{ORR})^{-1}$ represents the effective resistance of the ORR, which is decomposed into six terms on the right hand side designated as R_1 to R_6, respectively. Therefore, the ORR can be represented as a series of resistances. Within the serial resistor network a rate determining term (RDT) can be identified.

Figure S2 shows the rate constants k_i of elementary reaction steps as functions of E. Figure 5 displays the separate resistive terms R_i on the

right hand side of Eq.(18) as functions of E, calculated with parameters in the case of pH = 1.2. $R_1 = (K_3^* K_4^* k_1^*)^{-1}$ dominates in regime I for$E >$ 0.86 V. $R_2 = (K_4^* k_1^*)^{-1}$ dominates in regime II for 0.84 V $< E <$ 0.86 V. $R_3 = (k_1^*)^{-1}$ dominates in regime III when $E <$ 0.84 V. The consecutive transitions from R_1 to R_2 and further to R_3 with decreasing E have important consequences on the effective rate of the ORR, and the differential Tafel slope (see next section).

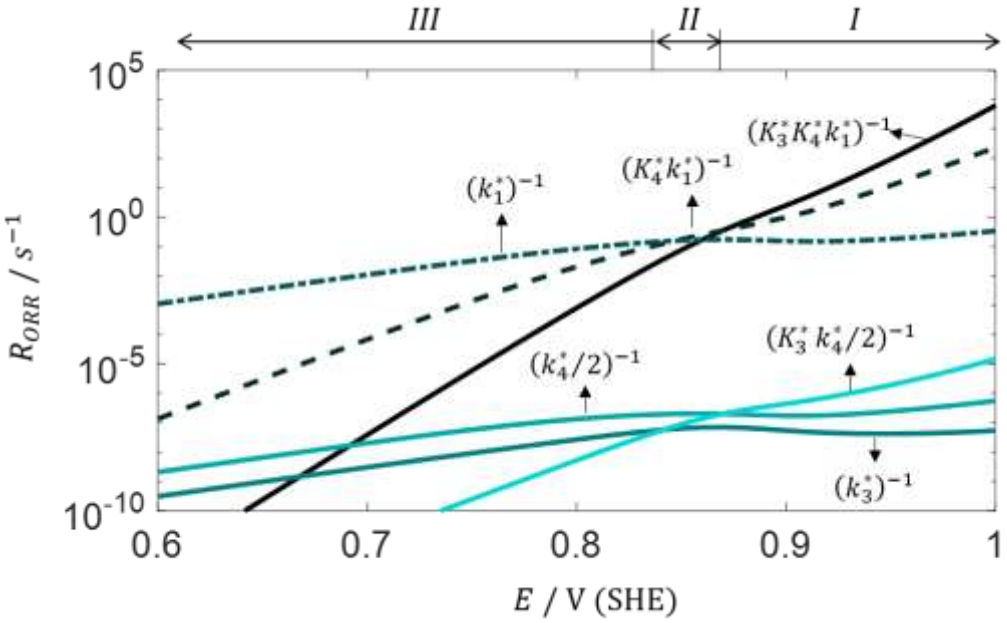

Figure 5. Rate-determining term of the ORR rate expression for the case of pH=1.2 in Figure 3.

3.4 Differential Tafel slope and exchange current density

A wealth of studies, from Pt single crystals to commercial Pt/C catalysts, have reported that the differential Tafel slope b increases from < 60 mV dec^{-1} to ~120 mV dec^{-1} with decreasing E from 1.0 V to 0.6 V.[4, 20, 22, 25, 35, 42] Table S2 selects representative results from the literature. It is usually believed that the site-blocking effect and negative energetic effect of chemisorbed oxygen intermediates are the root

causes of the potential-dependent Tafel slope.[22, 25, 35] Holewinski and Linic demonstrated that it is an inherent attribute of multi-step heterogeneous electrocatalytic reactions, using microkinetic modelling.[43]

In the preceding subsection, we found that the RDT of the ORR rate changes with varying E. The denominator of the dominating resistance in $(v_{\mathrm{ORR}})^{-1}$ has, in general, the form, $(K_3^*)^{\nu}(K_4^*)^{\mu}k_{\mathrm{i}}^*$, with the exponents ν, $\mu = 0$ or 1. Therefore, the intrinsic differential Tafel slope is given by,

$$b = \frac{2.3RT}{F}\frac{1}{\nu + \mu + 0.5}. \tag{25}$$

For the case of Figure 5, we have, (1) $\nu = \mu = 1$, $b \cong 24$ mV dec^{-1}when $E > 0.86$ V; (2) $\nu = 0$, $\mu = 1$, $b \cong 40$ mV dec^{-1} when 0.84 V $< E <$ 0.86 V; (3) $\nu = \mu = 0$, $b \cong 120$ mV dec^{-1} when $E < 0.84$ V. This simple analysis demonstrates that the potential-dependent Tafel slope can be traced back to transitions between RDT of the ORR rate.

An apparent differential Tafel slope is conveniently calculated as,

$$b_{app} = -\frac{\partial E}{\partial \log|j_{ORR}|}. \tag{26}$$

Given b_{app}, the exchange current density, j_{ORR}^0, can be calculated from the ORR current using the following equation,

$$j^0 = j_{ORR} \cdot 10^{\frac{E - 1.23\ \mathrm{V}}{b_{app}}}. \tag{27}$$

Figure 6 shows j^0 and b_{app} as functions of *E*. Over the potential range of interest for the ORR, i.e., for 0.6 V < E < 1.0 V, j^0 exhibits a marked increase with decreasing E, which explains the wide range of values found in experimental studies and is consistent with the general observation that that reported values are highly sensitive to the potential range employed for the Tafel analysis.[22, 44, 45] In addition, the surface charging effect increases j^0 in the high potential range by 1-3

orders of magnitude. Regarding b_{app}, the increasing trend with decreasing E is also in line with aforementioned experimental results. Values displayed in Figure 6 (b) for the Pt(111) electrode[28] (blue symbol) align very well with the theoretically obtained curve that accounts for the surface charging effect.

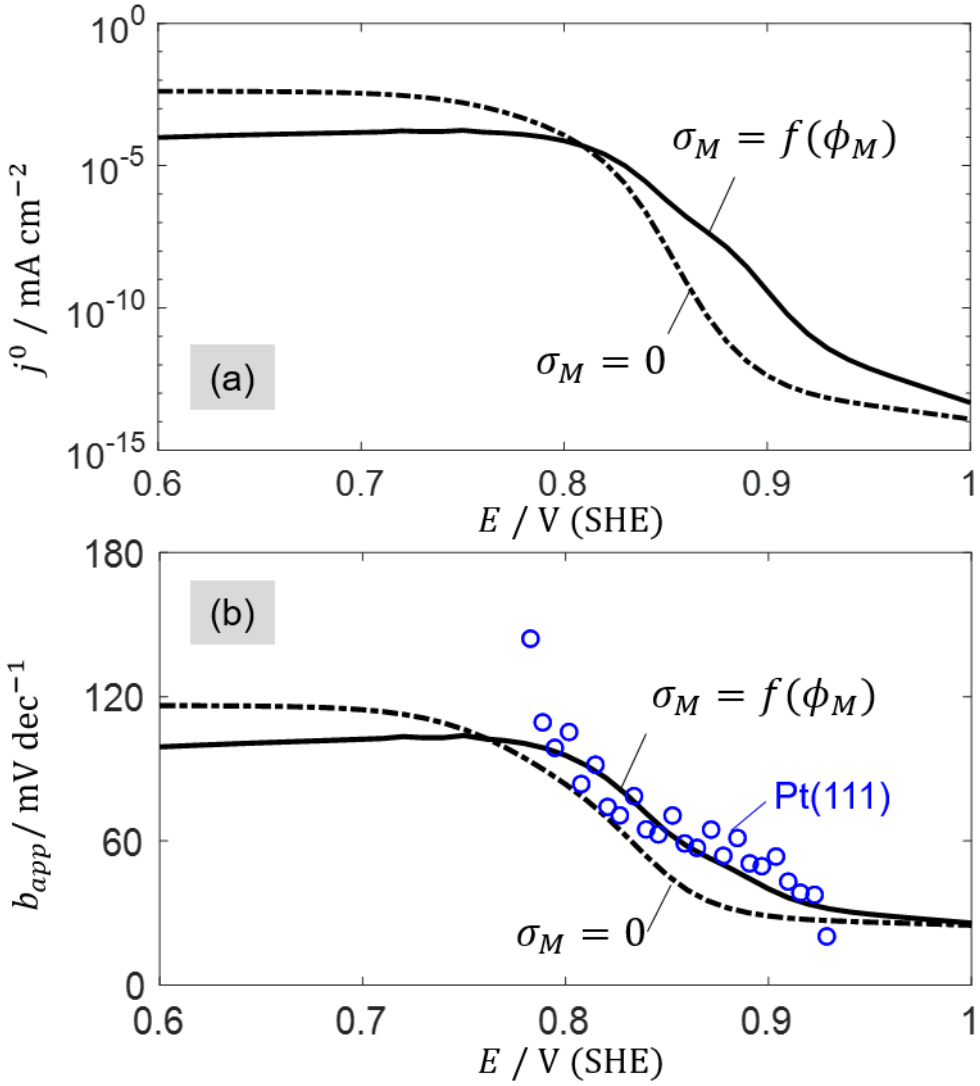

Figure 6. Exchange current density (a) and apparent differential Tafel slope (b) for the case of pH=1.2. For comparison, results are shown also for the case without surface charge effect, $\sigma_M = 0$, in dashed lines. The experimental Tafel slope data are corresponding to a Pt(111) electrode in $NaF/HClO_4$ electrolyte saturated with O_2 of 1 bar at room

temperature.[28]

3.5 Volcano plot

Binding energies of chemisorbed oxygen intermediates are interrelated.[41] Therefore, the hydroxyl binding energy, ΔG^0_{OH}, is usually employed as the sole descriptor of the ORR activity. Figure 7 compares the model with experimental data in terms of the relation between ORR activity and ΔG^0_{OH}. Experimental data are taken from Stephens *et al.* who collected the data from original studies in refs [18, 46-51]. In Figure 7(a), model results have been calculated using $\Delta G^{\mathrm{Pt},0}_{\mathrm{OH}} = 0.75$ eV and $\Delta G^{\mathrm{Pt},0}_{\mathrm{O}} = 1.65$ eV,* while keeping other parameters unaltered with their base values in Table 1 and 2 and S1. The dashed line corresponds to the case without surface charge effect, $\sigma_{\mathrm{M}} = 0$. The model curve with account of the surface charging effect neatly envelopes the experimental data. In addition, model and experiment are consistent in the location of the peak at $\Delta G^0_{\mathrm{OH}} - \Delta G^{\mathrm{Pt},0}_{\mathrm{OH}} = 0.1$ eV as well as the height of the peak.

For comparison, the case without surface charging effect, viz. assuming $\sigma_{\mathrm{M}} = 0$ is shown in Figure 7 as well. If the surface charging relation of the catalyst, which defines the local reaction conditions, is not accounted for, the peak of the ORR activity is shifted to larger ΔG^0_{OH} and the magnitude of the peak is overestimated by a significant factor,

* We found this modification necessary to achieve a good agreement between model and experimental data. Moreover, parametric analysis indicates that the location of the peak is controlled by $\Delta G^{\mathrm{Pt},0}_{\mathrm{OH}}$ and $\Delta G^{\mathrm{Pt},0}_{\mathrm{O}}$ while $\Delta G^{\mathrm{Pt},0}_{\mathrm{OOH}}$ has a minor effect. A recent DFT study of He *et al.* revealed that solvation energies contribute significantly to the binding energies of reaction intermediates. Specifically, the error brought by assuming identical solutions for different catalysts can be up to 0.21-0.24 eV.[41] This finding provides a plausible explanation for the change in binding energies used in Figure 7 compared with that in Figure 3.

approximately by a factor 5. Increasing $\Delta G_{\mathrm{OH}}^{0}$ decreases θ_{OH} and θ_{O}, see Figure S3. In the low range of $\Delta G_{\mathrm{OH}}^{0}$, chemisorbed oxygen species are strongly bonded to the electrode surface, that is, $\theta_{\mathrm{OH}} + \theta_{\mathrm{O}} \approx \theta_{\mathrm{max}}$, implying that the site-blocking effect will dominate. As a consequence, decreasing θ_{OH} and θ_{O} by increasing $\Delta G_{\mathrm{OH}}^{0}$ leads to improvement in the ORR activity. When the surface charging effect is taken into consideration, lower θ_{OH} and θ_{O} increases σ_{M} towards positive values, hence, decreasing the interfacial proton concentration and the ORR activity. A quantitative analysis will be given in section 4.1.

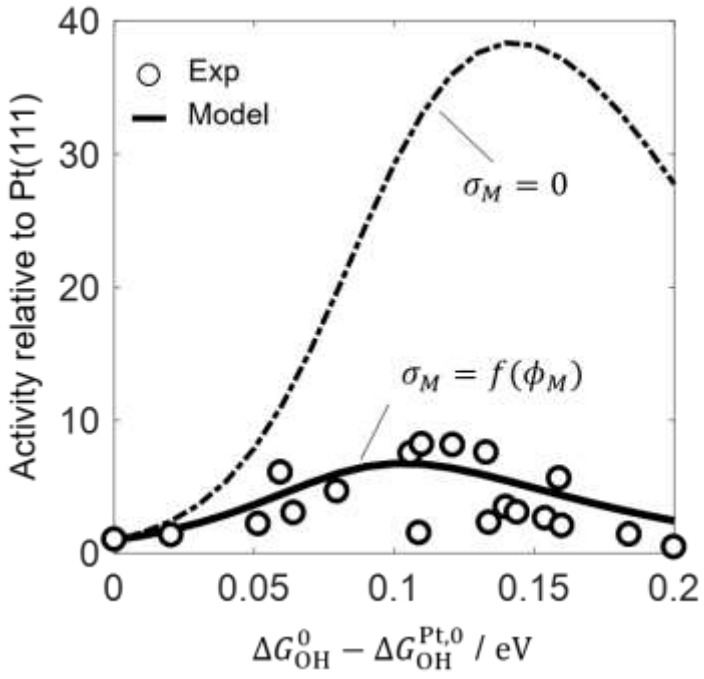

Figure 7. Volcano plot for different Pt-catalysts with different hydroxyl binding energies, $\Delta G_{\mathrm{OH}}^{0}$. The ORR activity is relative to that of Pt(111). All activity data are calculated at $E = 0.9$ V (RHE). The adjusted model parameters are $\Delta G_{\mathrm{OH}}^{\mathrm{Pt},0} = 0.75$ eV, $\Delta G_{\mathrm{O}}^{Pt,0} = 1.65$ eV and other parameters have their base values. Experimental data are taken from the review in ref 1. The dashed line in (a) corresponds to the case without surface charge effect, $\sigma_{\mathrm{M}} = 0$.

4 DISCUSSION

4.1 Root causes of volcano plot

From Eq.(18) it is seen that the dominating contribution to the effective ORR resistance has the general form, $(K_3^*)^\nu(K_4^*)^\mu k_\mathrm{i}^*$ with the exponents $\nu, \mu = 0$ or 1, and $i = 1, 3, 4$. It is interesting to note that we have two different types of quantities at play, namely the thermodynamic quantity K_i^* and the kinetic quantity k_i^*. As detailed in the supporting information, we set Pt(111) as the reference, and express K_i^*, k_i^* and hence v_ORR as a function of $\left(\Delta G_\mathrm{OH}^0 - \Delta G_\mathrm{OH}^{\mathrm{Pt},0}\right)$, the abscissa of the volcano plot,

$$v_\mathrm{ORR} \propto \exp\left((\nu(\zeta_\mathrm{O} - 1) + \mu - \zeta_i) \frac{\Delta G_\mathrm{OH}^0 - \Delta G_\mathrm{OH}^{\mathrm{Pt},0}}{RT} \right), \tag{28}$$

with,

$$\zeta_i = \begin{cases} \beta_1 \zeta_\mathrm{OOH}, & i = 1 \\ -\beta_3(\zeta_\mathrm{O} - 1), & i = 3 \\ -\beta_4, & i = 4 \end{cases} \tag{29}$$

where $\zeta_\mathrm{O} = 2$, $\zeta_\mathrm{OOH} = 1$ and $\beta_i = 0.5$. Note that we have dropped the potential-dependent terms as the volcano plot analysis corresponds to a specific potential. It is emphasized that these potential-dependent terms are also implicit functions of ΔG_OH^0.

Eq.(28) indicates: (1) if $\nu(\zeta_\mathrm{O} - 1) + \mu > \zeta_i$, v_{ORR} increases exponentially with increasing $\left(\Delta G_\mathrm{OH}^0 - \Delta G_\mathrm{OH}^{\mathrm{Pt},0}\right)$; (2) if $\nu(\zeta_\mathrm{O} - 1) + \mu < \zeta_i$, v_{ORR} decreases exponentially with increasing $\left(\Delta G_\mathrm{OH}^0 - \Delta G_\mathrm{OH}^{\mathrm{Pt},0}\right)$. As a result, the volcano plot essentially reflects the shift from $\nu(\zeta_\mathrm{O} - 1) + \mu > \zeta_i$ to $\nu(\zeta_\mathrm{O} - 1) + \mu < \zeta_i$. The volcano plot, namely the above shift, is possible only when the $\zeta_i = \beta_1 \zeta_\mathrm{OOH}$, that is, the first step is the step with the highest

activation barrier.† Otherwise, $\nu(\zeta_{\mathrm{O}}-1)+\mu-\zeta_i$ is always positive regardless of $\left(\Delta G_{\mathrm{OH}}^{0}-\Delta G_{\mathrm{OH}}^{\mathrm{Pt},0}\right)$.

Here we illustrate a concrete example for above theoretical analysis. Regarding the case with model parameters all having their base values, RDTs for two different catalysts with $\left(\Delta G_{\mathrm{OH}}^{0}-\Delta G_{\mathrm{OH}}^{\mathrm{Pt},0}\right)=0$ and 0.2 eV are analyzed, respectively. For the case of $\left(\Delta G_{\mathrm{OH}}^{0}-\Delta G_{\mathrm{OH}}^{\mathrm{Pt},0}\right)=0$ on the left wing of the volcano plot, the RDT is $R_1=(K_3^*K_4^*k_1^*)^{-1}$ at 0.9 V (RHE), as shown in Figure S4 (a). In this case, $\nu(\zeta_{\mathrm{O}}-1)+\mu-\zeta_i=1.5$, hence, v_{ORR} increases exponentially with increasing $\left(\Delta G_{\mathrm{OH}}^{0}-\Delta G_{\mathrm{OH}}^{\mathrm{Pt},0}\right)$, according to Eq.(28). In contrast, the RDT shifts towards $R_3=(k_1^*)^{-1}$ when increasing $\left(\Delta G_{\mathrm{OH}}^{0}-\Delta G_{\mathrm{OH}}^{\mathrm{Pt},0}\right)$ towards 0.2 eV, as shown in Figure S4 (b). In this case, $\nu(\zeta_{\mathrm{O}}-1)+\mu-\zeta_i=-0.5$, hence, v_{ORR} decreases exponentially with increasing $\left(\Delta G_{\mathrm{OH}}^{0}-\Delta G_{\mathrm{OH}}^{\mathrm{Pt},0}\right)$.

4.2 ORR activity vs. coverage of adsorbed oxygen intermediate

Given the same parameter set used in Figure 7(a), Figure 8 plots the simulated correlation between the normalized total coverage, $\tilde{\theta}_{OX}=(\theta_{OH}+\theta_O)/\theta_{max}$, of chemisorbed oxygen intermediates and the normalized ORR activity at 0.9 V (RHE). Several representative electrocatalysts are located in the plot.

For the case of $\sigma_{\mathrm{M}}=0$, the ORR activity slightly increases with $\tilde{\theta}_{OX}$ in the low coverage range $[0, 0.65]$ and then decreases in the high coverage range $[0.65, 1.0]$. In this scenario, the non-monotonic relation results

† Earlier literature designated this step as a rate determining step;[17,22] however, we consider this label as misleading and avoid using it since other steps are similarly important (or more important if considered together) in determining the effective ORR rate. Therefore, we rather promote the concept of a rate-determining term as discussed in Section 3.3.

from the interplay of two competing effects: on the one hand, chemisorbed oxygen species are reaction intermediates of the ORR and reactants of steps (3) and (4); on the other hand, they act as site-blockers of step (1). For the case that accounts for the surface charging effect, the ORR activity increases with $\tilde{\theta}_{OX}$ in the low coverage range $[0, 0.85]$ and it decreases sharply at high oxide coverage $[0.85, 1.0]$. It is the protophilic effect that shifts the location of the ORR activity peak from 0.65 to 0.85. The model predicts that the optimal electrocatalyst should have a $\tilde{\theta}_{OX}$ of 0.85, mainly contributed by OH^* (see Figure S3).

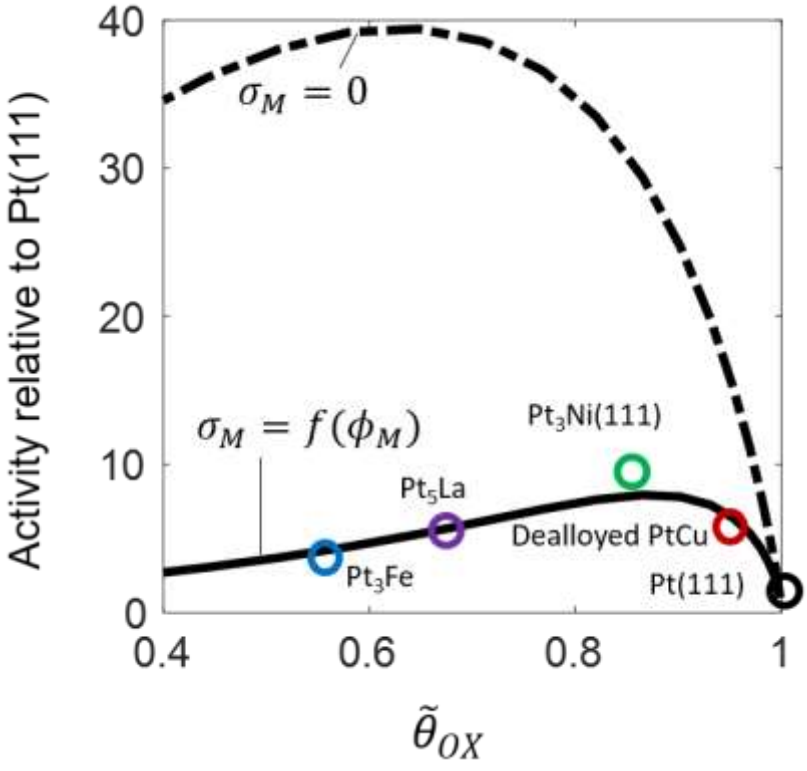

Figure 8. The relation between ORR activity and total coverage of chemisorbed oxygen intermediates normalized to θ_{max} (the maximum fraction of lattice sites that could be covered with chemisorbed oxygen intermediates), $\tilde{\theta}_{OX} = (\theta_{OH} + \theta_O)/\theta_{max}$. All activity data are calculated at $E = 0.9\ V$ (RHE) using the same parameter set as in Figure 7.

Experimental data are taken from the review.[1] The dashed line corresponds to the case without surface charging effect, $\sigma_M = 0$.

4.3 Key parameters of the ORR

As many model parameters ought to be determined by DFT, it is important to identify the main influencing parameters and gauge their impact on ORR performance. Herein, parametric analysis is conducted using the exchange current density and the Tafel slope as analytical tools. Four parameters, including binding energies, $\Delta G_{OH}^{Pt,0}$, $\Delta G_{O}^{Pt,0}$ and $\Delta G_{OOH}^{Pt,0}$, and partial charge number of Pt-oxide, χ, are examined in Figure 9.

Regarding the exchange current density curve, $\Delta G_{OH}^{Pt,0}$ and $\Delta G_{O}^{Pt,0}$ have major influence on the shape, while $\Delta G_{OOH}^{Pt,0}$ only raises or lowers the curve without changing its shape. Specifically, $\Delta G_{OH}^{Pt,0}$ and $\Delta G_{O}^{Pt,0}$ dominate in the low and high potential range, respectively. In terms of the Tafel slope curve, $\Delta G_{OH}^{Pt,0}$ exerts a marked effect on the transition from the lower plateau at ca. 30 mV/dec to the upper plateau at ca. 90 mV/dec. Increasing $\Delta G_{OH}^{Pt,0}$ by 0.05 eV shifts the transition to higher potentials by ca. 50 mV. Increasing χ_{OH} means amplifying the effect of surface oxide dipoles. As seen in Figure 9 (g), the exchange current density is enlarged with increasing χ_{OH} and a peak emerges at ca. 068 V, at which potential σ_M drops to negative values. Correspondingly, a peak at the same potential is seen in the Tafel slope curve.

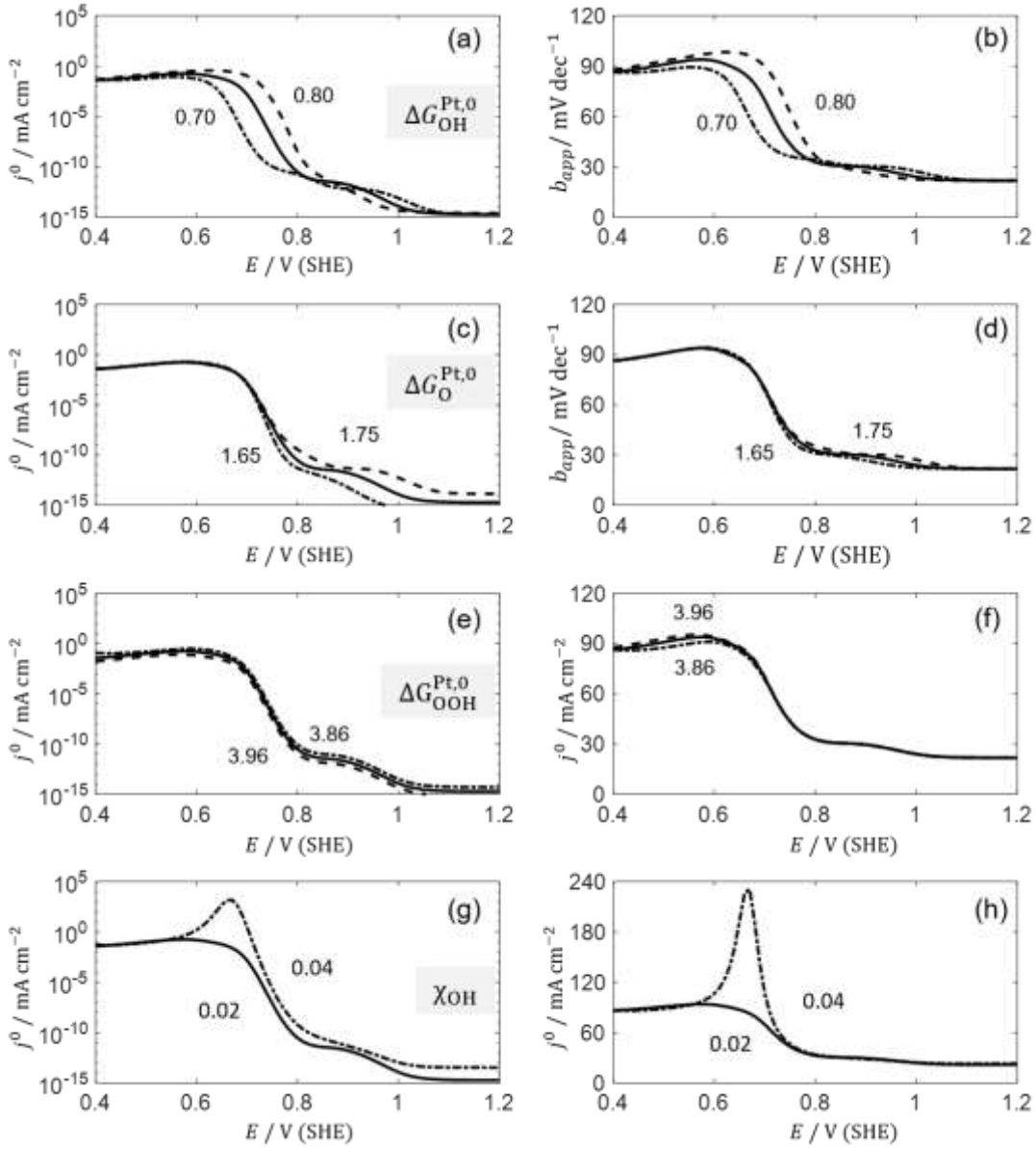

Figure 9. Effect of (a)(b) $\Delta G_{OH}^{Pt,0}$, (c)(d) $\Delta G_{O}^{Pt,0}$, (e)(f) $\Delta G_{OOH}^{Pt,0}$, (g)(h) χ_{OH} on the exchange current density and the Tafel slop curve corresponding a Pt(111) electrode in 0.1 M $HClO_4$ at room temperature. One parameter is changed at a time, while others have their base values for each curve.

5 CONCLUSIONS

This article presents a theoretical framework for deciphering the ORR

based on a unified treatment of the formation of chemisorbed oxygen intermediates, surface charging effects, thermodynamics and kinetics of the ORR. Double-layer effects have been incorporated into ORR theory for the first time. Using a basic experimentally bolstered parameterization, the established formalism gives an expression for the inverse rate of the ORR that can be deconvoluted into a series of resistive terms; the rate-determining term is proposed as a new concept that should replace the classical rate-determining step for multi-electron processes. Moreover, it yields the effective Tafel slope and exchange current density as continuous functions of the electrode potential and refines the perspective for a descriptor-based evaluation of catalyst activity. It is demonstrated that the non-monotonic metal charging relation exerts a marked impact on the ORR activity, by tuning the protophilicity at the electrode-electrolyte interface. The non-linear coupling between the formation of chemisorbed oxygen species and surface charge density exerts a marked impact on the Volcano-type relation for the catalyst activity.

One important message conveyed in this study is that the electrostatic effects at the scale of the Debye length (<10 nm) are crucial albeit non-trivial for the understanding of Pt electrocatalysis, in addition to the geometric and electronic factors at the atomic scale (0.1~1 nm) and mass transport factors at the electrode scale (>0.1 μm). This model can be an important module in a hierarchical modeling framework to rationalize electrocatalytic phenomena in complex electrodes for polymer electrolyte fuel cells and electrolyzers, complementing DFT studies of reaction mechanisms and pathways at the lower end and porous electrode theory at the upper end of the spectrum of scales.

ACKNOWLEDGEMENT

J Huang appreciates financial support from the starting fund for new faculty members at Central South University (502045001). J Zhang gratefully acknowledges financial support from National Natural Science Foundation of China under the grant number of U1664259. M. Eikerling gratefully acknowledges financial assistance through an Automotive Partnership Canada grant, file number APCPJ417858, that supports the Catalysis Research for Polymer Electrolyte Fuel Cells(CaRPE-FC) network.

CONFLICTS OF INTEREST

There are no conflicts to declare.

REFERENCES

1. I. E. L. Stephens, A. S. Bondarenko, U. Gronbjerg, J. Rossmeisl and I. Chorkendorff, *Energy Environ. Sci.*, 2012, **5**, 6744-6762.
2. M. J. Eslamibidgoli, J. Huang, T. Kadyk, A. Malek and M. Eikerling, *Nano Energy*, 2016, **29**, 334-361.
3. M. Watanabe, D. A. Tryk, M. Wakisaka, H. Yano and H. Uchida, *Electrochim. Acta*, 2012, **84**, 187-201.
4. A. M. Gomez-Marin, R. Rizo and J. M. Feliu, *Catal. Sci. Technol.*, 2014, **4**, 1685-1698.
5. M. Wakisaka, H. Suzuki, S. Mitsui, H. Uchida and M. Watanabe, *Langmuir*, 2009, **25**, 1897-1900.
6. M. Wakisaka, Y. Udagawa, H. Suzuki, H. Uchida and M. Watanabe, *Energy Environ. Sci.*, 2011, **4**, 1662-1666.
7. H. S. Casalongue, S. Kaya, V. Viswanathan, D. J. Miller, D. Friebel, H. A. Hansen, J. K. Nørskov, A. Nilsson and H. Ogasawara, *Nat. Commun.,* 2013, **4**, 2817.
8. Z. Zeng and J. Greeley, *Nano Energy*, 2016, **29**, 369-377.
9. J. K. Nørskov, J. Rossmeisl, A. Logadottir, L. Lindqvist, J. R. Kitchin, T. Bligaard and H. Jónsson, *J. Phys. Chem. B*, 2004, **108**, 17886-17892.
10. J. Rossmeisl, A. Logadottir and J. K. Nørskov, *Chem. Phys.*, 2005, **319**, 178-184.

11. G. S. Karlberg, J. Rossmeisl and J. K. Norskov, *Phys. Chem. Chem. Phys.*, 2007, **9**, 5158-5161.
12. V. Tripković, E. Skúlason, S. Siahrostami, J. K. Nørskov and J. Rossmeisl, *Electrochim. Acta*, 2010, **55**, 7975-7981.
13. H. A. Hansen, V. Viswanathan and J. K. Nørskov, *J. Phys. Chem. C*, 2014, **118**, 6706-6718.
14. J. Chen, L. Fang, S. Luo, Y. Liu and S. Chen, *J. Phys. Chem. C*, 2017, **121**, 6209-6217.
15. M. T. M. Koper, *J. Electroanal. Chem.*, 2011, **660**, 254-260.
16. V. Viswanathan, H. A. Hansen, J. Rossmeisl and J. K. Nørskov, *ACS Catal.*, 2012, **2**, 1654-1660.
17. M. Busch, N. B. Halck, U. I. Kramm, S. Siahrostami, P. Krtil and J. Rossmeisl, *Nano Energy*, 2016, **29**, 126-135.
18. V. R. Stamenkovic, B. Fowler, B. S. Mun, G. Wang, P. N. Ross, C. A. Lucas and N. M. Marković, *Science*, 2007, **315**, 493-497.
19. N. M. Marković, H. A. Gasteiger, B. N. Grgur and P. N. Ross, *J. Electroanal. Chem.*, 1999, **467**, 157-163.
20. E. J. Coleman and A. C. Co, *ACS Catal.*, 2015, **5**, 7299-7311.
21. A. Damjanovic and V. Brusic, *Electrochim. Acta*, 1967, **12**, 615-628.
22. D. B. Sepa, M. V. Vojnovic and A. Damjanovic, *Electrochim. Acta*, 1981, **26**, 781-793.
23. D. B. Sepa, M. V. Vojnovic, L. M. Vracar and A. Damjanovic, *Electrochim. Acta*, 1987, **32**, 129-134.
24. J. X. Wang, F. A. Uribe, T. E. Springer, J. Zhang and R. R. Adzic, *Faraday Discuss.*, 2009, **140**, 347-362.
25. N. P. Subramanian, T. Greszler, J. Zhang, W. Gu and R. R. Makharia, *ECS Trans.*, 2011, **41**, 985-1007.
26. M. Wakisaka, H. Suzuki, S. Mitsui, H. Uchida and M. Watanabe, *J. Phys. Chem. C*, 2008, **112**, 2750-2755.
27. A. M. Gómez–Marín and J. M. Feliu, *J. Solid State Electrochem.*, 2015, **19**, 2831-2841.
28. V. Briega-Martos, E. Herrero and J. M. Feliu, *Electrochim. Acta*, 2017, **241**, 497-509.
29. J. Huang, A. Malek, J. Zhang and M. H. Eikerling, *J. Phys. Chem. C*, 2016, **120**, 13587-13595.
30. A. N. Frumkin and O. A. Petrii, *Electrochim. Acta*, 1975, **20**, 347-359.
31. J. Huang, J. Zhang and M. Eikerling, *Faraday Discuss.*, 2016, **193**, 427-446.
32. J. A. Keith and T. Jacob, *Angew. Chem., Int. Ed.*, 2010, **49**, 9521-9525.
33. M. P. Hyman and J. W. Medlin, *J. Phys. Chem. B*, 2005, **109**, 6304-6310.
34. J. Rossmeisl, G. S. Karlberg, T. Jaramillo and J. K. Norskov, *Faraday Discuss.*, 2009, **140**, 337-346.
35. J. X. Wang, J. Zhang and R. R. Adzic, *J. Phys. Chem. A*, 2007, **111**, 12702-12710.

36. N. Garcia-Araez, V. Climent and J. Feliu, *J. Phys. Chem. C*, 2009, **113**, 9290-9304.
37. V. Climent, R. Gómez, J. M. Orts and J. M. Feliu, *J. Phys. Chem. B*, 2006, **110**, 11344-11351.
38. A. Malek and M. H. Eikerling, *Electrocatal.*, 2017, DOI: 10.1007/s12678-017-0436-0.
39. J. M. Bockris, M. A. Devanathan and K. Muller, *Proc. Royal Soc. A*, 1963, **274**, 55.
40. J. Huang, A. Malek, J. Zhang and M. H. Eikerling, *J. Phys. Chem. C*, 2017, **121**, 26140-26140.
41. Z.-D. He, S. Hanselman, Y.-X. Chen, M. T. M. Koper and F. Calle-Vallejo, *J. Phys. Chem. Lett.*, 2017, **8**, 2243-2246.
42. N. Markovic, T. Schmidt, V. Stamenkovic and P. Ross, *Fuel Cell*, 2001, **1**, 105-116.
43. A. Holewinski and S. Linic, *J. Electrochem. Soc.*, 2012, **159**, H864-H870.
44. A. Parthasarathy, S. Srinivasan, A. J. Appleby and C. R. Martin, *J. Electrochem. Soc.*, 1992, **139**, 2856-2862.
45. A. Parthasarathy, S. Srinivasan, A. J. Appleby and C. R. Martin, *J. Electrochem. Soc.*, 1992, **139**, 2530-2537.
46. J. Zhang, M. B. Vukmirovic, Y. Xu, M. Mavrikakis and R. R. Adzic, *Angew. Chem., Int. Ed.*, 2005, **44**, 2132-2135.
47. V. Stamenkovic, B. S. Mun, K. J. Mayrhofer, P. N. Ross, N. M. Markovic, J. Rossmeisl, J. Greeley and J. K. Nørskov, *Angew. Chem.*, 2006, **118**, 2963-2967.
48. GreeleyJ, I. E. L. Stephens, A. S. Bondarenko, T. P. Johansson, H. A. Hansen, T. F. Jaramillo, RossmeislJ, ChorkendorffI and J. K. Nørskov, *Nat. Chem.*, 2009, **1**, 552-556.
49. W.-P. Zhou, X. Yang, M. B. Vukmirovic, B. E. Koel, J. Jiao, G. Peng, M. Mavrikakis and R. R. Adzic, *J. Am. Chem. Soc.*, 2009, **131**, 12755-12762.
50. P. Strasser, S. Koh, T. Anniyev, J. Greeley, K. More, C. Yu, Z. Liu, S. Kaya, D. Nordlund, H. Ogasawara, M. F. Toney and A. Nilsson, *Nat. Chem.*, 2010, **2**, 454-460.
51. I. E. L. Stephens, A. S. Bondarenko, F. J. Perez-Alonso, F. Calle-Vallejo, L. Bech, T. P. Johansson, A. K. Jepsen, R. Frydendal, B. P. Knudsen, J. Rossmeisl and I. Chorkendorff, *J. Am. Chem. Soc.*, 2011, **133**, 5485-5491.